Design and manufacture of large aperture wavefront sensor

Rich Hutchin[*a], Oberdan Otto[a], Alan Wertheimer[b]
[a]Optical Physics Company, 26610 Agoura Road, Calabasas, CA USA 91302
[b]Eastman Kodak Company, 1447 St. Paul Street, Rochester, NY USA 14653-9521

ABSTRACT

A compact, low-cost wavefront sensor has been demonstrated to measure dynamic disturbances in 1–3 m diameter optical systems. With 448 subapertures and 4 kHz frame rate, it can measure disturbances up to 2 kHz at a level of 1/3800 waves rms at 0.65 µm. It also has a linear dynamic range of 3×10^6:1 for ease of alignment. The principles of operation and test data are presented for the subaperture sensors (called NanoTrackers), which are lateral shearing interferometers capable of measuring tilt to 1.7 nanoradians rms at 8 µW of input power as well as phasing for segmented optical systems to 75 picometers rms (at 4 kHz).

Keywords: Wavefront sensor, large aperture, high accuracy, low cost

1.0 INTRODUCTION

There are a growing number of large optic programs in the world, such as the 6.5 m James Webb Space Telescope and 10+ m designs for space-based lasers. Large optical systems such as these require equally large test systems, which diagnose and verify end-to-end optical performance. Making a diffraction-limited 10-meter test system can be a huge expense and require extraordinarily large vacuum test chambers. With this need in mind, Optical Physics Company (OPC) has designed a compact and modular wavefront sensor (Fig. 1) that can be hung over, beside, or positioned under the operational system. It can measure absolute wavefront (including absolute focus and phasing errors) to 1/100 wave rms and dynamic disturbances up to 2 kHz at 1/4000 wave rms. A typical cost is \$600K/m^2 for a dynamic wavefront sensor plus 20% for absolute wavefront capability.

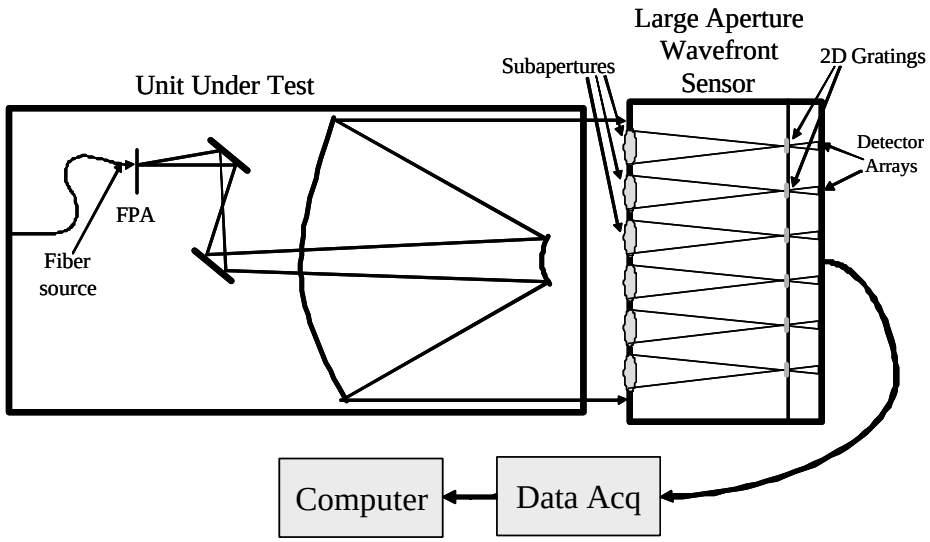

Fig. 1. Configuration of the modular wavefront sensor to test a large optical system.

* corresponding author's email; phone; fax

In order to use this wavefront sensor, one or more fiber sources are placed at the focus of the optical system under testing. A fiber source makes a high-quality point source that propagates through the system and out the primary mirror to the Large Aperture Wavefront Sensor (LAWS) modules. The wavefront measured represents a complete single pass through the entire optical system. No other alteration, besides adding a fiber source, is required for the system under test, which makes this testing approach very easy to integrate into any optical system. After testing, the fiber source can be removed.

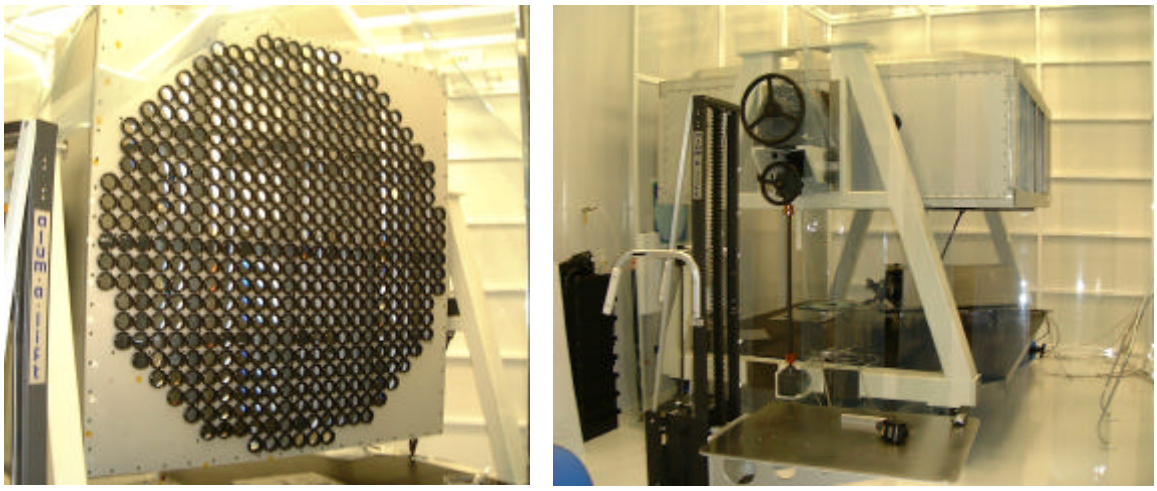

Fig. 2. The first LAWS module with a 2.4 m test diameter in vertical and horizontal configurations.

The first module, shown in Fig. 2, with a 2.4 m test area was delivered to Eastman Kodak Company in December 2003 and underwent acceptance testing in January 2004 [see companion paper 5553-33 in this Proceedings]. It was designed to be an AC sensor only and did not incorporate our newer absolute wavefront technology.

2.0 DESCRIPTION OF LAWS SYSTEM

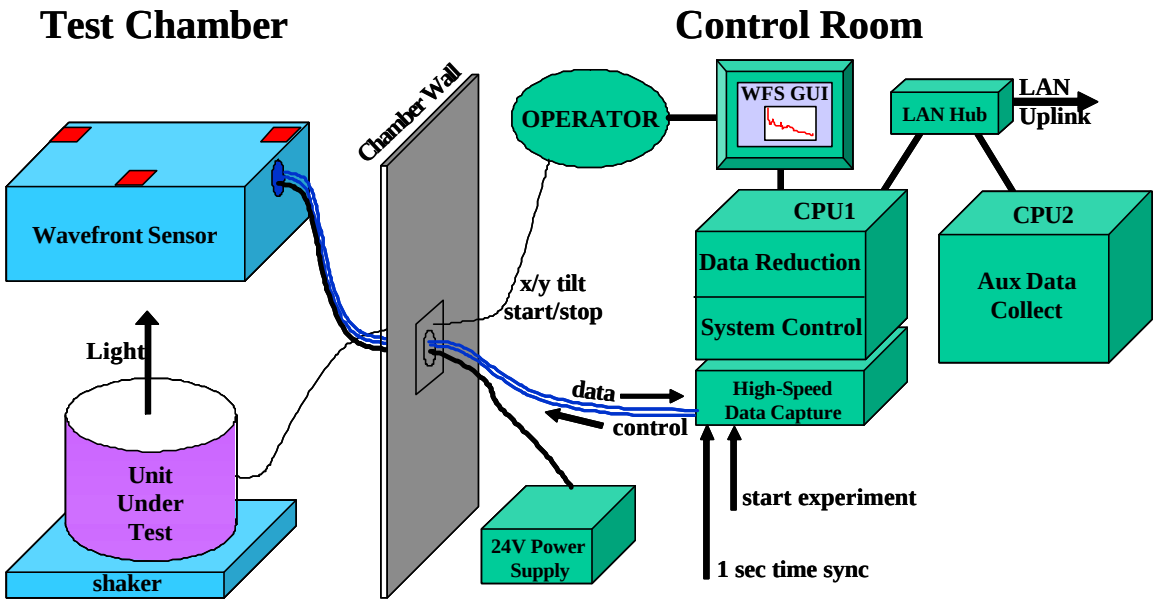

Fig. 3. Layout of the modular sensor with the unit under test.

The LAWS system shown in Figs. 1 and 2 uses a two-dimensional shearing interferometer in each subaperture to measure the subaperture tilt or phasing error. While the sensor is discussed in detail in Sec. 3.0, its main advantages are very low rms noise (λ/4000 rms), high bandwidth (4 kHz), large linear dynamic range (3×10^6:1) for easy alignment and phasing measurements between adjacent segments of λ/5000 rms. The output of these sensors are measured using custom focal planes fabricated for OPC by Hamamatsu Corporation, digitized, muxed, and transmitted through a cable out of the vacuum test chamber, as shown in Fig. 3.

The 4 kHz subaperture data is passed through the vacuum wall to a high-speed data acquisition disk. External 1 s time markers and a start acquisition signal allow the WFS data set to be precisely synchronized with other data systems. Once a data collect (up to 4.5 h long) is complete, portions of the data can be reviewed to see PSDs and time histories. This Quick Look data review is designed to determine whether the last collect was likely to be correctly implemented. Next, the entire set is processed to extract the subaperture tilt data and it is passed to other user-specific routines for further analysis.

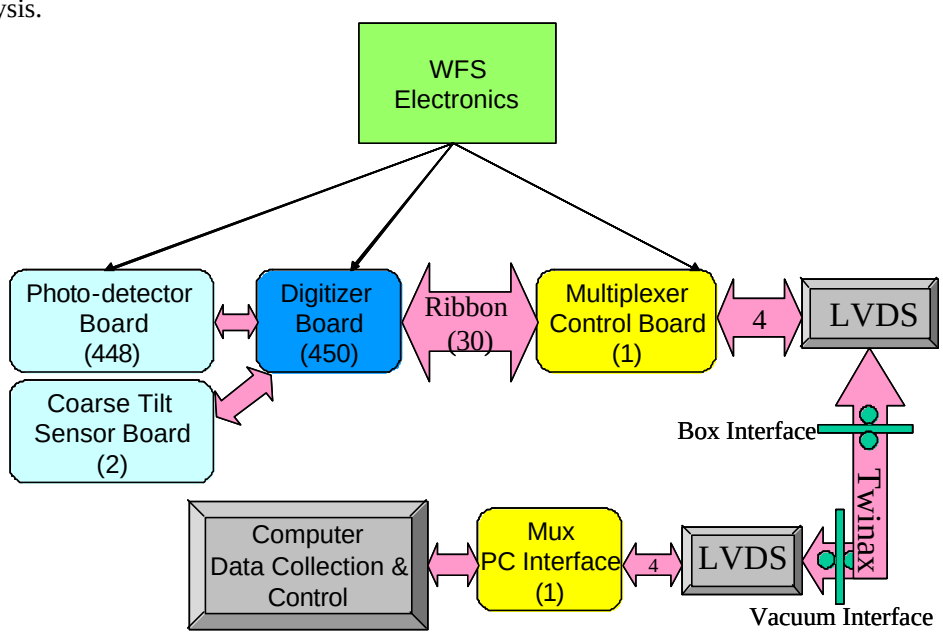

Fig. 4. WFS electronics schematic diagram.

All actions of the wavefront sensor from startup through calibration, data collection, Quick Look, and exporting are controlled by an intuitive Graphical User Interface (GUI). An example of a typical GUI display is shown in Fig. 5.

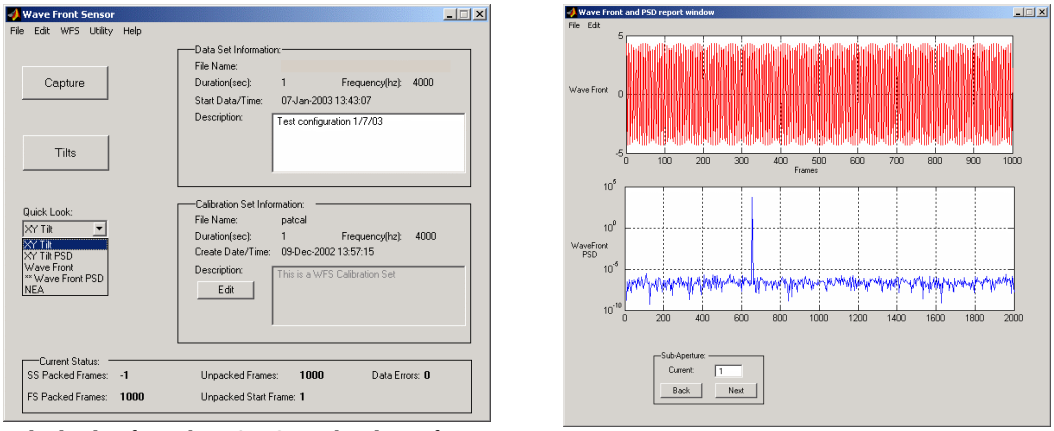

Fig. 5. Sample display from the LAWS graphical interface.

3.0 NANOTRACKER SENSOR

The heart of the wavefront sensor is the NanoTracker shown in Fig. 4.

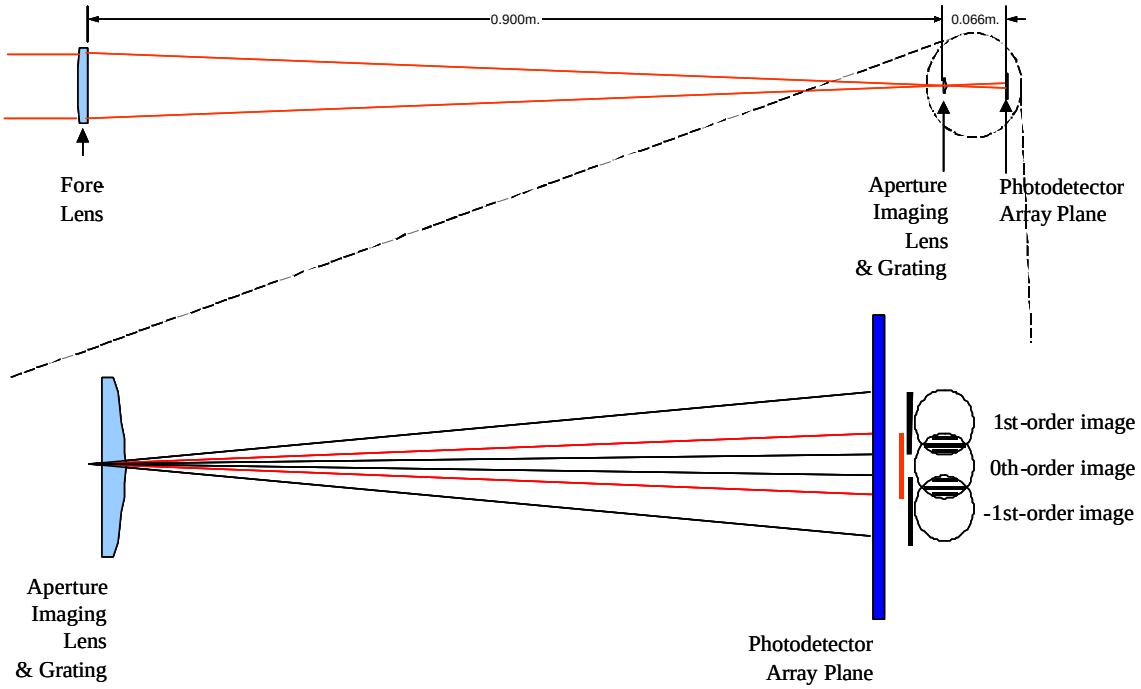

Fig. 6. Optical design of the NanoTracker used in each subaperture. A is the full sensor, and B is a magnification of the grating-detector area.

The NanoTracker is a lateral shear interferometer (LSI) with a focusing lens (fore lens), a plano-convex aperture-imaging lens, a 2-D grating on the planar side of the plano-convex lens, and a photodetector array. The fore lens focuses light from the input wavefront onto the grating. The plano-convex lens. Thereafter, images the fore lens (entrance aperture) onto the detector array. The resulting image convolves the original image with the Fourier transform of the grating, which produces overlapping and interfering copies of the entrance aperture. The detector consists of two 4-element 1-D arrays that sample the fringes in the interference pattern to determine its phase.

The grating of the lateral shear interferometer has a 2-D checkerboard pattern, as illustrated in Fig. 7c. This grating pattern has a 75% average transmission rate of incident light. Figs. 7a–7d illustrate the beam intensity patterns as light propagates within the lateral shearing interferometer of Fig. 6. Figure 7a illustrates the uniform intensity of light from the wavefront as it enters the fore lens. Figure 7b illustrates the intensity of light focused down to a small spot just prior to the grating. Figure 7c illustrates the intensity pattern of light just after transmitting through the grating where the inverse checkerboard pattern has blocked regions of the light. Figure 7d illustrates the intensity pattern of light at the detector plane, which is conjugate to the fore lens.

Note that the period of the grating (16.8 μm) is chosen to shear the beam by 62% of the input diameter in the first order. This makes the zero and first orders overlap but entirely removes the higher orders from the pattern. In addition, the X and Y overlap areas are substantially disjointed to facilitate precise phase measurements of each axis.

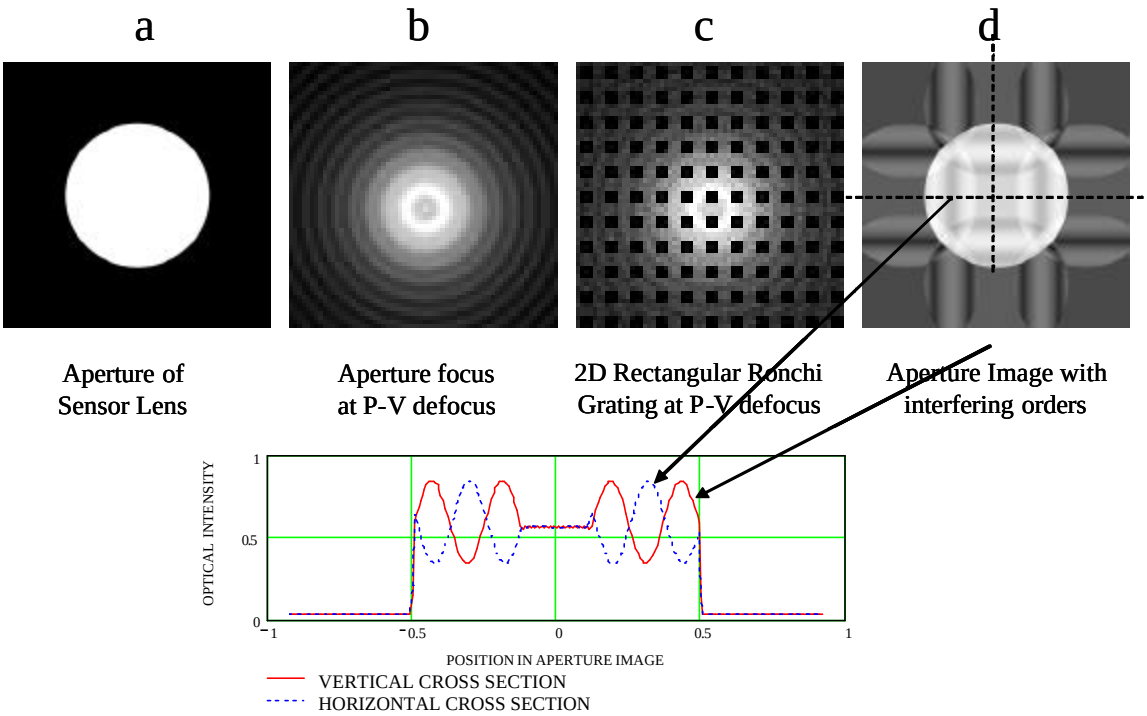

Fig. 7. The beam intensity patterns are shown here for the NanoTracker from the entrance aperture (a), to just before the 2-D grating (b), to just after the 2-D grating (c), to the detector plane (d). X and Y cuts across the intensity pattern at the detector are also plotted.

The formula for the amplitude of each order of the 2-D grating is given by the following equations:

Amp(j,k) = 0.75 if j = k = 0;
Amp(j,k) = $1/(\pi^2 jk)$ if both j and k are odd;
Amp(j,k) = $1/(2\pi j)$ if j is odd and k = 0;
Amp(j,k) = $1/(2\pi k)$ if k is odd and j = 0; and
Amp(j,k) = 0 for all other values of j and k.

These amplitudes satisfy the conservation-of-energy principle because the sum of their squares is 0.75, which is the transmission of the checkerboard-grating pattern. Each order gives a translated image of the uniformly illuminated pupil whose intensity is proportional to the square of the strength of the order. The intensity of the image for each order is the grating efficiency for that order. Thus, where the amplitude of the zero order image (j = k = 0) is 0.75, the grating efficiency is 0.75^2 = 56.3% of light at the aperture of the lateral shear interferometer, and where the strength of the first order image (j = k = 1) is $1/(2\pi)$, the grating efficiency is 2.5%.

Figure 8 illustrates an enlarged image of the lateral shear interferometer aperture on the focal plane. The central disk is the higher intensity zero-order image of the primary lens, having 56.3% of the light entering the subaperture of the lateral shear interferometer less any optical losses. The four first-order images are positioned at 90° intervals around the zero-order image, each with 2.5% of the light, relative to light, entering the subaperture of the lateral shear spectrometer. Overlapping regions are created where the first-order images overlap the zero-order image. Within these overlapping regions, the images interfere to make fringes having approximately a 40% modulation in intensity. Figure 7 shows a plot illustrating the modulation of light in the fringes resulting from the overlap of the zero-order and first-order images.

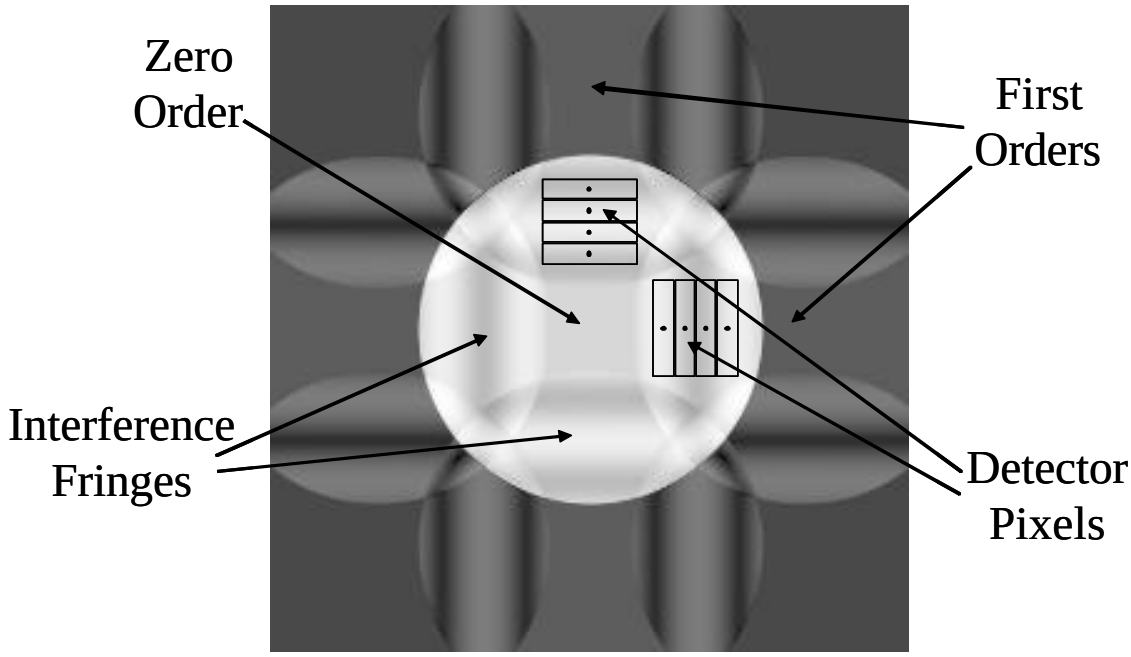

Fig. 8. Expanded view showing the light distribution at the detector plane. The zero-order image of the entrance aperture is about 5 mm in diameter.

The period of the modulation is inversely proportional to the amount of defocus of the light at the grating. Thus, by controlling the spacing between the fore lens and the grating, a full period of modulation may be created within the fringe of the zero-order image and any first-order image, as shown in Fig. 8. The four pixels in each 1-D detector array can now spatially sample the fringe every 90° in phase. This gives quadrature components that can be used to estimate the phase of the fringe very accurately. The phase is computed by summing the four pixel intensities, S_j, multiplied by complex weights W_j. The phase of the resulting complex number is the phase of the spot centroid on the grating.

$$\phi_{tilt} = \arg\left[\sum_{j=0}^{3}\left(Wt_j \cdot S_j\right)\right] \tag{1}$$

where arg(z) = phase of the complex number z, S_j = the four pixel intensity values, and W_j = complex weights determined by the calibration process described in Sec. 3.

This algorithm is applied to X and Y data for all subapertures in the sensor. Since that phase of each fringe is perfectly linear in the tilt of the beam, this detection system has excellent linearity over a very wide range (set by the size of the grating). The phase of interference in the fringes varies by exactly 360° when the spot focused on the grating moves by a full grating period.

The light source chosen for the first module has a wavelength, λ, in the near infrared band at 0.852 μm. The diameter of the subaperture, D, is 7 cm with a focusing lens having a focal length, F, of 90 cm. The power, P, of light from the 0.852-μm source received by each subaperture of the wavefront sensor is approximately 6 μW.

In selecting the period of the grating, one is choosing how much overlap, or shear, occurs between the different order images on the detector. Preferably, the shear is selected as approximately 2/3 of a fore lens diameter; however, other shear values may also be used. A good shear may be obtained by selecting a grating period, p, for which λ/p equals 2/3

of the tangent of the cone angle for light focused onto the grating. Thus, the grating period for this example is approximated by

$$p = \frac{3\lambda \cdot F}{2D} = 16.4\ \mu m \quad . \tag{2}$$

The system delivered to Eastman Kodak Company had a period of 16.8 µm, which gave a shear of 65% of the subaperture beam diameter.

The next parameter chosen is the reimaging focal length of the plano-convex lens. This focal length is chosen so that an appropriately sized image of the subaperture of the linear shear interferometer is created on the detector. The goal is to size the image so that the desired number of detector elements fall within the overlap regions. The image preferably has a diameter of about 4–5 mm on the detector (for convenience in making the silicon chip), creating an overlap region that is approximately 1/3 of the image of the fore lens. This image and overlap region size is a reasonable size for a silicon-based detector and simplifies alignment of the image with the detector elements. To produce an image of this size, a plano-convex lens is chosen with a focal length, F, of 6 cm. The resulting zero-order image has a diameter, d_0, of approximately 4.67 mm because the size of the zero-order image is the size of the fore lens aperture (70 mm) times the ratio of the focal length of the plano-convex lens divided by the focal length of the fore lens (6 cm/90 cm). The overlap region thus has a size of approximately 1.55 mm along the major axes of the zero-order image.

The intensity of light incident upon the detector is dependent upon the transmission of the primary and plano-optical lenses and the grating efficiency. In this module, the combined transmission rate of the primary and plano-optical lenses, τ, is about 90%. As indicated above, the grating has an efficiency, eff0, of 56.3% for the zero-order image and an efficiency, eff1, of 2.5% for each first-order image. In the overlap regions, the apparent efficiency of the grating is the sum of the efficiencies for the zero- and first-order images.

A modulation factor in the fringes is also determined for the fringe regions. The modulation factor multiplies the signal-to-noise –ratio (SNR) and is therefore a factor determining the performance of the lateral shear interferometer. The definition for modulation is the difference in intensity of light between the peak and the minimum, divided by the sum of the peak and the minimum in the fringes, as the spot of light moves across one period of the grating. Since the grating amplitudes multiply the input light amplitude to give the amplitude on the focal plane, they add and subtract for constructive and destructive interference, and are squared to convert them from amplitude to intensity. Thus, the modulation factor, γ, is given by the following equation:

$$g = \frac{\left((\mathrm{eff}_0)^{\frac{1}{2}} + (\mathrm{eff}_1)^{\frac{1}{2}} \right)^2 - \left((\mathrm{eff}_0)^{\frac{1}{2}} - (\mathrm{eff}_1)^{\frac{1}{2}} \right)^2}{\left((\mathrm{eff}_0)^{\frac{1}{2}} + (\mathrm{eff}_1)^{\frac{1}{2}} \right)^2 + \left((\mathrm{eff}_0)^{\frac{1}{2}} - (\mathrm{eff}_1)^{\frac{1}{2}} \right)^2} \approx 0.40 \quad ? \tag{3}$$

To continue setting up the lateral shear interferometer, the detector is positioned at the desired distance, 6 cm as indicated above, from the plano-optical lens so that four detector elements are within at least two of the fringes, as shown in Fig. 8. The four detector elements are preferably well within the bounds of the fringes so that precise alignment is not required. Once the detector elements are positioned, however, stability of the alignment is desirable. The modulation period of light in the fringe is selected so that one period is equal to the width of the four detector elements. In this module, a single detector has a width of 0.22 mm and a length of 0.78 mm, so the combined width, Δ, of the four detectors is 0.88 mm, and we set to set the fringe period, pf, to 0.88 mm to sample an entire modulation period with the four detector elements.

As previously indicated, the modulation period of light in the fringe is proportional to the amount of defocus of light from the fore lens relative to the grating. The amount of defocus required, Δz, is given by the following equation:

$$\Delta z = \frac{l F^2 \cdot d_0}{p_f D^2 (Shr)} \approx 1.11 \text{ mm} \tag{4}$$

where Shr is the desired shear amount of 2/3 in this example.

With the above parameters determined, the average amount of power received by a single detector element, Pd, may be calculated by the following equation:

$$P_d = \frac{P \cdot t \cdot (eff_0 + eff_1) A_d}{p d_0^2 / 4} \approx 28 \text{ nanoWatts} \tag{5}$$

where P is the power of light from the light source, and Ad is the area of a single detector element. The amount of power received by each detector element may be multiplied by the responsivity of the detector element and the integration time, and divided by the charge of an electron to arrive at the total signal in photoelectrons. For purposes of this example, the responsivity, η, of a silicon-based detector is assumed to be 0.35 amp/W (conservative) and the measurement time, Δt, is 0.5 ms. The responsivity and measurement time may vary depending upon the type of detector used and the measurement bandwidth required. Thus, the average number of photoelectrons, N_{ph}, is 3.3×10^7 photoelectrons measured per sample time by each detector element in this example.

The total noise of the resulting signal measurement is the root sum square of the shot noise and the readout noise. The total signal, divided by this total noise, gives the signal-to-noise ratio, SNR, and allows an estimate of performance to be calculated. The SNR is calculated as an average over a full cycle. Such an approach is appropriate because measurements from all four detector elements are used to calculate the fringe phase along each axis of the zero-order image.

For this module, the detector readout noise, N_d, is about 3000 photoelectrons. The SNR of each detector element is

$$SNR_d = \frac{N_{ph}}{\sqrt{N_{ph} + (N_d)^2}} \approx 5090 \tag{6}$$

Because the total number of detector elements, N_{det}, is four in each fringe region, the total signal-to-noise ratio, SNR_{tot}, of the detector within each fringe region is given by the following equation:

$$SNR_{tot} = g \cdot SNR_d \cdot (N_{det})^{\frac{1}{2}} \approx 4070 \tag{7}$$

where γ is the signal modulation factor determined previously.

Fringe measuring systems have a root mean square (RMS) accuracy in radians given by root(2)/SNR_{tot}. This RMS formula is standard for shearing interferometers and has been well validated experimentally. Thus, the phase accuracy, σ_ϕ, of a single measurement using the lateral shear interferometer in this example is approximately 3.5×10^{-4} rad. This result may be scaled to determine the RMS accuracy of the tilt measurement along one axis using the following equation:

$$s_t = \left(\frac{3l}{2D}\right) \cdot \left(\frac{s_f}{2p}\right) \approx 1.0 \text{ nanoradians} \tag{8}$$

Therefore, each lateral shear interferometer of the wavefront sensor described herein can achieve a noise level of around 1 nrad RMS using conventional detectors and sources. The primary reason for this high performance is that a lateral shear interferometer measures the tilt angle modulo of an angle equal to the wavelength divided by the shear distance, which is set at 2/3 of the subaperture diameter in this example. Thus, with a 7 cm subaperture, the tilt angle is measured modulo $\lambda/(D \cdot Shr)$ rad, which is about 18 μrad. Therefore, in lateral shear interferometers, a signal-to-noise ratio of approximately 2000, or more, places the RMS_{tilt} noise in the low nanoradian range.

It is important to remember that a shearing interferometer measures phase only modulo 2π. However, as long as the sampling rate is fast enough so that the beam tilt never moves more than about 1/3 of a grating period between samples, the motion can be tracked continuously over many cycles. For a wavefront sensor designed to measure dynamic disturbances, this simple phase continuizing process is sufficient since the average value of each time sequence of tilt measurements will have its mean value subtracted in the processing. One can use this data to obtain spatial modes across the full aperture, power spectral densities (PSDs), and covariant spectral densities (CSDs).

To be specific, the time history of phase readings across multiple cycles may be continuized using the following algorithm. If P_J is the time sequence of phase measurements in cycles, the missing integer portion may be added by assuming that the first lateral shear interferometer measurement is in the 0–1 range and tracking the cycle shifts with the following equation, which adds in the integer portion to each subsequent measurement, J+1, starting at J = 0 and running consecutively through the entire time history:

$$P_{J+1} = P_{J+1} + \mathrm{NINT}(P_J - P_{J+1}), \tag{9}$$

where NINT(x) is a function that provides the nearest integer of the argument x.

Using the above equation, if $P_{200} = 29.377$ after continuizing and $P_{201} = 0.4078$, this equation will reset P_{201} to 29.4078. Also if $P_{200} = 29.941$ and $P_{201} = 0.1162$, this equation will reset P_{201} to 30.1162. This happens because 30.1162 is closer to 29.941 than 29.1162 and is, statistically, a more likely correct answer.

3.0 NANOTRACKER CALIBRATION

The above-described wavefront sensor assumes that the lateral shear interferometers of each subaperture have been calibrated so that when comparisons of the tilt measurements between subapertures are performed, the comparisons provide a meaningful and accurate results. Four different types of calibration are preferably performed on the wavefront sensor:

1. Pixel dark calibration
2. Pixel phase calibration
3. Gain calibration of the NanoTracker
4. Rotation calibration of the NanoTracker;

Pixel calibration is performed to ensure the precision of the fringe-phase estimation. There are 8 pixels per subaperture (4 X and 4 Y pixels). Each pixel is first calibrated in DC bias. This is a standard type of sensor processing. All light is blocked to get the zero input values, which are subtracted from all subsequent data. By removing the zero bias, the sensor will become immune to fluctuations in the wavefront intensity since the algorithm.

Pixel-phase calibration is performed so that the relative intensity, modulation, and phase offset of each pixel may be accurately determined. The process is to input a smoothly tilting beam to each subaperture, perhaps at a 45° orientation to the X/Y shear directions so that both X and Y tilts are generated simultaneously. This allows both X and Y sensors to be calibrated simultaneously. Each sensor sees a smoothly varying sinusoidal intensity pattern with time. That pattern is truncated to the nearest integer number of cycles and Fourier transformed. The largest non-DC peak of the transform is the tilt signal with magnitude M and phase ϕ.

The DC level, DC_j, the magnitude, M_j, and the phase, ϕ_j of each pixel signal, j, is recorded and used to compute noise-optimized complex weights that are applied to the later data to estimate the fringe phase for each frame of data. The phase estimation weights are calculated using the following three equations for the four unknown weights, Wt_j:

$$\sum_{j=1}^{4} Wt_j \cdot DC_j = 0 \quad , \tag{10}$$

$$\sum_{j=1}^{4} Wt_j \cdot M_j \cdot e^{li \cdot f_j} = e^{li \cdot f_2} \quad \text{, and} \tag{11}$$

$$\sum_{j=1}^{4} \left(\left| Wt_j \right| \right)^2 \quad \text{is minimized.} \tag{12}$$

The solution to the above equations uses LaGrange multipliers and minimizes the error metric E shown in the following equation:

$$E = \sum_{j=1}^{4} \left(\left| Wt_j \right| \right)^2 - m \cdot \sum_{j=1}^{4} Wt_j \cdot DC_j - n \cdot \left(\sum_{j=1}^{4} Wt_j \cdot M_j \cdot e^{li \cdot f_j} - e^{li \cdot f_2} \right) \tag{13}$$

The solution to the unknown weights may be determined to be:

$$Wt_k = \frac{-\left(\sum_{j=1}^{4} DC_j \cdot M_j \cdot e^{-li \cdot f_j} \right) \cdot e^{li \cdot f_2} \cdot DC_k + \left[\sum_{j=1}^{4} \left(DC_j \right)^2 \right] \cdot e^{li \cdot (f_2 - f_k)} \cdot M_k}{\left[\sum_{j=1}^{4} \left(DC_j \right)^2 \right] \cdot \left[\sum_{j=1}^{4} \left(M_j \right)^2 \right] - \left(\sum_{j=1}^{4} DC_j \cdot M_j \cdot e^{-li \cdot f_j} \right)^2} \tag{14}$$

The purpose of the above weight equations is to sum weights times the signals from the four pixels that are sampling one fringe. The result is a complex number whose phase is the phase of the fringe. This is a normal sort of four-bin processing often used for interferometers. In eq. (14), the optimized weight is determined for each fringe. In eq. (13), the error metric uses the LaGrange multipliers μ and ν. Equation (10) is the weight requirement that rejects the DC level, and eq. (11) is the weight requirement that determines the proper phase from the AC portion of the signal. When eq. (12) is at a minimum, this weight requirement minimizes the impact of RMS noise on the LSI measurement. Assuming the noise is uniform and uncorrelated (e.g., white noise), this last condition means that the weights are chosen so the sum of their squares with the impact of noise is minimized.

Gain calibration is the next step. The LSI does not measure tilt directly, it measures phase of an interference pattern in cycles. One cycle of phase corresponds to a particular amount of external tilt (in radians) depending upon the focal length of the lens, the amount of defocus, and the period of the grating. These parameters may vary somewhat from subaperture to subaperture, so each subaperture must be calibrated separately in each axis to determine the multiplicative factor relating its phase measurement to external tilt at the entrance lens.

The gain calibration consists of inputting a known sweep in X and/or Y tilt and dividing the known tilt change with the measured phase shift in cycles. This scale factor is stored for each axis and each subaperture. Rotation calibration of the fine sensor is performed because the grating and sensor in each subaperture may not have been placed at the same angle relative to the gratings and sensors of the other subapertures. Therefore, the gratings and sensors of each subaperture are likely to have a slight relative rotation. This means that each subaperture has its own definition of X and Y. In order to combine the data meaningfully from all the subapertures together, the data must be de-rotated.

The rotation calibration may be accomplished by illuminating the entire focal plane at once and tilt the beam along one axis at a time. Each subaperture is likely to have different amounts of X and Y response. Typically, if one is moving the beam in the nominal X direction, all the X sensors have nearly the same response because the error in the X direction is a cosine term based on the rotation. For this reason, the X direction error between subapertures is often negligible. However, the response in the Y direction is linear relative to the rotation and is easily observed.

As an example, suppose that under nominal X tilt, the X sensor of subaperture A sees its fringe move 112.3774 fringes, while the Y sensor sees its fringes move 1.2317 fringes. The rotation of the sensor is given by ArcTan(–1.2317/112.3774), and the sensor is rotated 0.6280 degrees clockwise. Since this is being done simultaneously for all subapertures, the relative rotation of each subaperture may be accurately determined. Typically, the average of all the sensors is defined as the zero rotation point and each sensor's rotation is calculated as the deviation from the average.

A simple field calibration process may be performed by illuminating each subaperture with a beam that moves smoothly in a spiral, a raster pattern, or any other scan pattern that samples the entire photopot range at the desired spatial resolution. The outputs of the LSI are continuously recorded, and the scanning is done slowly enough that the LSI data does not change by more than 1/4 of a fringe from frame to frame. In this way, 2π changes in fringe phase can be resolved by time continuity, and a very precise and linear time history of the motion can be recorded.

4.0 PERFORMANCE RESULTS

The LAWS performed better than the 5 nrad rms requirement with a median rms noise of 1.7 nrad over the 2 kHz band. Figure 9 shows the noise histogram for all X and Y channels of 448 subapertures. We see that 97% were below 4.21 nrad, which, when rss'd with other error sources (such as expected seismic leakage), would give a total of 5 nrad. Finally, 99% were 10 nrad rms noise or less. All these tests were done at low light level (around 15% of saturation), and the noise performance of this sensor at its high illumination level (75% of saturation) is about 3X better.

After the wavefront data is taken, it is processed into subaperture tilts and reconstructed into an isometric plot of wavefront versus time, as shown in Fig. 9. This display can be played as a movie to show the dynamic response of the optical system to the input disturbances.

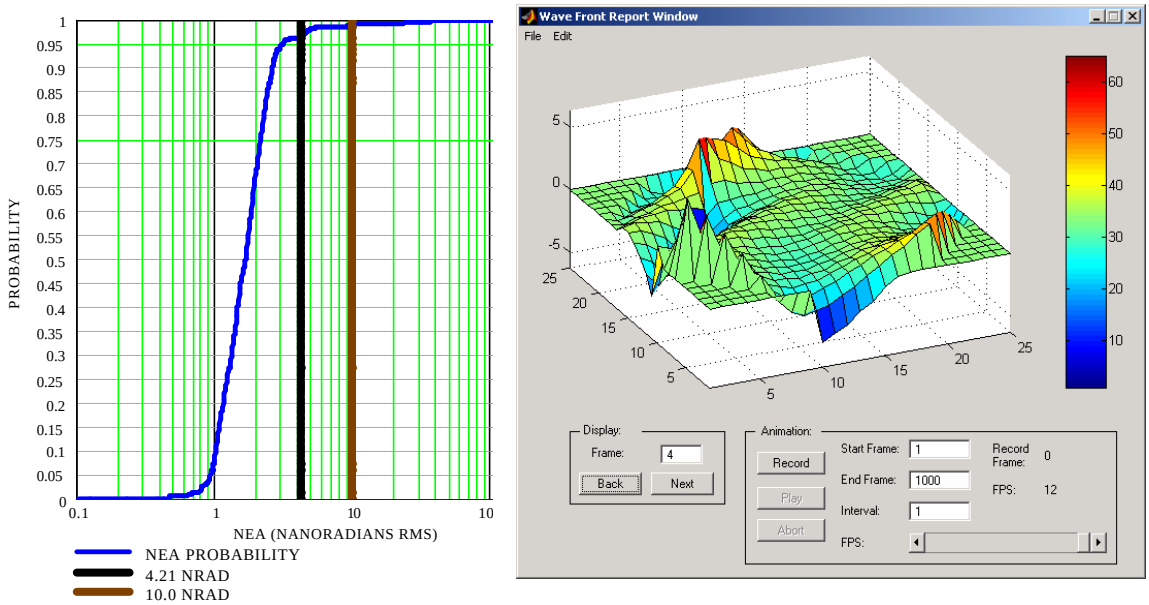

Fig. 9. Distribution of NanoTracker noise showing median noise of 1.7 nrad (left) plus a typical wavefront isometric plot (right).

Because the system was tested without seismic isolation, we picked up considerable seismic disturbance from the 101 Freeway, which is close to OPC, as shown in Fig. 10 (left). Much of our testing had to be done in the evenings and weekends to minimize this problem and verify the very low level of noise required. Figure 10 (right) shows a PSD taken on Sunday evening. Note that the disturbance below 800 Hz is considerably attenuated compared to the PSD taken during rush-hour traffic. One can also see in Fig. 10 the difference in the noise floor for high- and low-light level illumination conditions. The rush-hour data were taken with a light level of about 75% of saturation, and the weekend data set was taken with a low light level around 15% of saturation. High light level had a noise floor around 10^{-4} nanoradians^2/Hz and the low light level PSD had a noise floor of around $1x10^{-3}$ nanoradians^2/Hz.

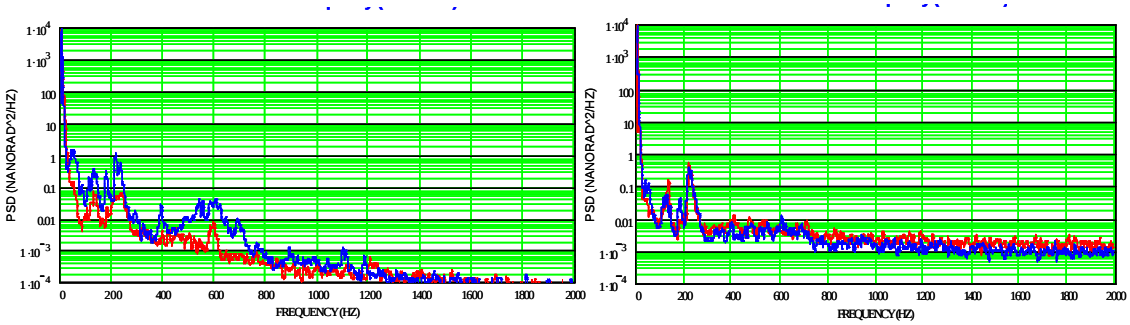

Fig. 10: Left plot shows a PSD from a NanoTracker during rush hour at 75% light level. Right plot shows a night-time PSD at 15% light level.

ACKNOWLEDGMENTS

We wish to thank Eastman Kodak Company for their technical support during the design, fabrication, and testing of this new sensor. Their close participation, technical insights, and creative suggestions played a significant role in the success of this project.

REFERENCES

Useful references on lateral shearing interferometers are:

J. W. Hardy, *Adaptive optics for Astronomical Telescopes*, Oxford University Press, New York, 1998.

R. K. Tyson, *Principles of Adaptive Optics*, Academic Press Inc., 1991.

References for wavefront reconstruction are:

J. W. Hardy, *Adaptive optics for Astronomical Telescopes*, Oxford University Press, New York, 1998.

R. K. Tyson, *Adaptive Optics Engineering Handbook*, Marcel Dekker Inc, New York, 2000.